Large-Angle Proton-Proton Elastic Scattering at Intermediate Momenta*†

R. C. Kammerud,‡ B. B. Brabson, R. R. Crittenden, R. M. Heinz,
H. A. Neal,§ H. W. Paik,‖ and R. A. Sidwell**
Indiana University, Bloomington, Indiana 47401
(Received 5 April 1971)

Differential cross sections have been measured for large-angle p-p elastic scattering at intermediate momenta in an experiment performed at the Argonne National Laboratory Zero Gradient Synchrotron. A wire-spark-chamber detection system was employed. The results are reported at 13 momenta between 1.5 and 5.5 GeV/c, and cover the angular region $30 \leq \theta_{\text{c.m.}} \leq 90°$. The statistical accuracy of the data, presented in 2° bins in $\theta_{\text{c.m.}}$, is typically ±4%. The data suggest slope changes in the fixed-$\theta_{\text{c.m.}}$ cross sections near $-t = 0.8$ and 3 (GeV/c)^2. The results of attempts to interpret the data in terms of optical models, the statistical model, the Regge-pole model, and a diffractive model are presented. A Regge calculation which predicts the masses at which dibaryon resonances might be expected to occur is outlined.

I. INTRODUCTION

The goal of this experiment was to make a detailed investigation of the large-angle differential cross section in p-p elastic scattering at intermediate momenta. This study has been prompted by the somewhat unusual or unexpected results of other experiments performed in recent years to investigate the p-p interaction. These include (1) the structure in the p-p polarization near $-t = 0.7$ (GeV/c)^2 observed by Neal and Longo[1] and later substantiated by Booth *et al.*,[2] (2) the small enhancement in the p-p total-cross-section measurements by Bugg *et al.*[3] at $P_L \approx 3$ GeV/c, (3) the appearance of a secondary diffraction-like shoulder in the CERN high-energy p-p angular-distribution data,[4-7] and (4) the rapid change in slope of the $\theta_{\text{c.m.}} = 90°$ cross sections near $-t = 6.5$ (GeV/c)^2 observed by Akerlof *et al.*[8]

This experiment was performed to search for any features in the angular distribution which may be correlated with the observed structure in the polarization and total-cross-section data, to determine the nature of the fixed-angle cross section at momenta below those of Akerlof *et al.*,[8] and to determine if secondary diffraction-like behavior persists at intermediate momenta. Data were collected at 13 incident proton momenta between 1.5 and 5.5 GeV/c in the c.m. angular region from 30° to 90° with datum points spaced at 2° intervals. Typical statistical accuracies of ±4% have been obtained. Partial results from this experiment have been reported in Ref. 9.

In Sec. II the experimental procedure is outlined, and the analysis of the data is described in Sec. III. The results are presented in Sec. IV, and Sec. V is devoted to the interpretation of the data.

II. EXPERIMENTAL METHOD

The experiment was performed in secondary beam number 1 of external proton beam I at the Argonne National Laboratory Zero Gradient Synchrotron. This is a doubly focused septum beam with a momentum spread of ≈1% full width at half-maximum (FWHM) and an uncertainty in the central momentum of less than 1%. During the experiment, the beam spill had a 600-msec duration and a repetition rate of approximately 1000 bursts per hour. The beam intensity varied 30 000 particles (≈15 000 protons) per burst at the lower momenta to 70 000 particles (≈50 000 protons) per burst at the higher momenta.

The detection system used in the experiment consisted of a combination of scintillation counters and wire spark chambers employing magnetostrictive readout.

A. Experimental Layout

A schematic of the layout of the equipment is shown in Fig. 1. The beam enters from the left and is incident on a 12-in.×1.75-in.-diam liquid-hydrogen target. The solid figures represent polystyrene scintillation counters and the open figures represent the spark chambers. The beam particles were detected by counters B_1 and B_2. Counter $\bar{A}_H$ had a 1-in.-diam hole through which the beam passed. This served as a beam halo anticounter which typically intercepted 5-15% of the beam. A gas threshold Čerenkov counter ($\bar{C}_G$) was used to logically separate protons from pions and leptons in the beam. A beam proton then satisfied the logic requirement $B_1B_2\bar{A}_H\bar{C}_G$.

Counters A_1, A_2, A_3, and A_4 (A_3 and A_4 were located above and below the target and are not shown

in Fig. 1) were anticounters which covered most of the solid angle not subtended by the detecting system. The scattered particles were detected by at least one counter in each of the two arrays (F_1, F_2, F_3, and S_1, S_2, S_3) located downstream of the spark chambers in the two final-state arms.

The logic signature which resulted in a trigger of the spark chambers was $B_1B_2\bar{A}_H\bar{C}_G FS\bar{A}$, where F, S, and $\bar{A}$ represent the inclusively ORed result of the respective individual array.

The laboratory polar-angle acceptance of the system was from about 5° to 43° in the F (fast-proton) arm and from 24° to 75° in the S (slow-proton) arm. This corresponds to a c.m. angular acceptance of at least $30° \lesssim \theta_{c.m.} \lesssim 90°$ at all momenta.

Elastic scatters in which counter F_1 is struck correspond to small center-of-mass angles (near $\theta_{c.m.} = 30°$). This is the region in which the cross section is relatively large at any particular energy. In order to increase the large-angle statistics without recording an exorbitant number of small-angle scatters, part of the run time at most momenta was used with F_1 not included in the logic.

B. Experimental Equipment

A total of twelve wire spark chambers were used in the experiment, the number being equally divided among the following three sets of active areas: 8 in.×8 in., 17 in.×23 in., and 28 in.×36 in. The chambers consisted of two parallel planes of wires separated by a $\frac{1}{2}$-in. G-10 phenolic (Fiberglas) frame. The respective wire directions in the two planes were orthogonal. The planes were made up of parallel wires (0.005-in.-diam tempered beryllium copper) with a separation of approximately 1 mm. A piece of 200-mesh stainless-steel wire cloth was placed adjacent to each plane of chamber wires in order to provide a uniform field within the chamber. In the experiment the chambers were oriented so that all chamber wires were vertical or horizontal; no provisions were made to directly resolve multiple-spark ambiguities.

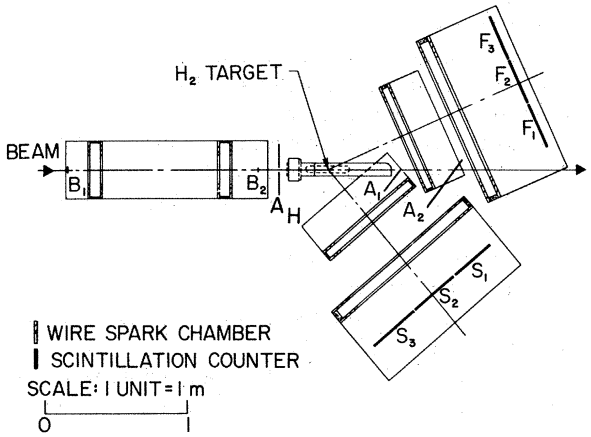

FIG. 1. The experimental layout.

During the experiment, the chambers were continuously purged with a mixture of 90% neon and 10% helium gas. In order to suppress spurious sparks, a small amount of isopropyl alcohol was introduced into the gas mixture before it entered the chamber. This was done by bubbling ~3% (by volume) of the gas through an alcohol bath at room temperature.

The spark-chamber trigger system consisted of a master spark-gap driver/amplifier which received the trigger command from the fast logic and in turn provided a spark trigger to each of six slave gaps, resulting in the application of a 7.5-kV high-voltage pulse to the chambers. A 100 V clearing field of opposite polarity to the pulse was maintained at all times in order to reduce the chamber memory time to about 1.5 μsec.

The resolution of the chambers was ~±1 mm. This was determined by investigating the deviation of sparks from fitted trajectories.

Prior to the beginning of the experiment, the efficiency of the individual chambers was measured by placing each chamber in a relatively low-intensity beam, defined by a scintillation-counter telescope, and comparing the counter-telescope rate with the reconstructed chamber event rate. This indicated an efficiency of about (90 ± 5)% for each chamber, and it was nearly constant over the active area of the chamber.

The magnetostrictive readout and recording system consisted of a Science Accessories Corporation digitizer interfaced with a Hewlett Packard digital tape deck. Four digitizing scalers were assigned to each spark-chamber plane. When the proper fast-logic requirements were satisfied, the master control unit signaled the tape transport to come to recording speed, and the contents of the data input units (fixed data, tagging units, accumulator scalers, and wire-spark-chamber scalers) were sequentially strobed onto magnetic tape. The tape transport operated in a continuous-write mode until the master control indicated that the end of scan had been reached. A total of approximately 20 000 events were recorded on each magnetic tape.

The experiment was monitored off-line using an Advanced Scientific Instruments Model 6020 computer. A program which read the magnetic tape and histogrammed the digitized scaler information was run several times daily. This provided a detailed check on chamber and readout-system operation.

In addition, the main analysis program was run periodically. This too served as a system-opera-

tion check and also gave some indication of the number of background events being accepted so that the run time at each momentum could be adjusted to meet the experimental goals.

III. ANALYSIS

The analysis of the data from this experiment was performed on the Indiana University Pattern Recognition Project's Sigma 5 computer, and it was conducted in four steps: (i) filtering and reconstruction, (ii) application of cuts and weighting of each event according to the geometric detection efficiency, (iii) background subtraction, and (iv) application of corrections to the data. These items will be discussed below. In addition, several methods have been used to check the internal consistency of the data. These will be briefly discussed in Sec. II E.

A. Filtering and Reconstruction

The main analysis program first searched each digitized wand output for the fiducial and counted the number of sparks observed by that wand. If no fiducial was found, this gap was assumed, in the remainder of the reconstruction, to have no sparks. It was demanded that of the four chambers in the beam arm, at least three recorded the passage of one and only one particle. If this condition was not met, the offending event was discarded and the total number of beam protons used in the calculation of the differential cross section was scaled down accordingly. The effect of this requirement was to eliminate events with possible multiple-beam tracks by eliminating about 5 to 10% of the recorded events. Of these discarded events, about half failed due to lack of sparks and the remainder due to scattering of sparks around a fitted line. This latter condition indicated that at least two beam particles entered the system and different chambers were responding singly to different particles. This procedure was not used on the arms detecting the final-state particles.

It was required that at least one of the two final-state detecting arms had at least two chambers with one and only one spark, so that vertex construction utilizing the beam trajectory was possible. In addition, the other arm must have had at least a single acceptable spark. Cases where there were less than two chambers in an arm with one and only one spark were rare and attributable to events of high multiplicity and to accidental coincidences in the F and S counters.

The interaction vertex was determined by the intersection of the trajectories in the beam arm and the final-state arm which had at least two chambers with one and only one spark. If both final-state arms satisfied this condition, the beam arm and slow arm (which makes the larger angle with the beam and therefore determines a vertex position more independent of the chamber resolution) were used. The three-dimensional locations of all possible combinations of sparks in the other arm were determined and elastic-scattering kinematics was used to select the spark lying closest to the trajectory corresponding to elastic scattering. The vector from the "known" vertex through this "selected" spark was then accepted as the true trajectory. All events were reconstructed in this manner. However, only ~3% of the final elastic events failed the more stringent requirement of having at least two chambers in each of the final-state arms with one and only one spark.

This procedure had the desirable effect of simplifying the analysis in that multiple tracks in a particular arm present many possible trajectories. This selection procedure permitted an immediate prediction of which of these trajectories should be used. The undesirable feature was that it tended to make randomly positioned sparks peak like elastic scatters; that is, it tended to draw background events toward the kinematic curve for elastic scattering. The careful manual reconstruction of many thousands of events verified that this did not present any significant problem. This was due primarily to the high chamber efficiency, to the small number of spurious sparks in the chambers, and the relatively small inelastic background.

B. Cuts and Detection Efficiency

The procedure used in placing the fiducial-volume cuts was (i) to discard all events for which the reconstruction indicated the particle passed within 1 in. of the inside edge of a spark-chamber frame, (ii) to discard all events for which the reconstruction indicated that the F and/or S counters were struck within $\frac{1}{2}$ in. or less of the outer counter edge, and, finally, (iii) to reject events occurring outside the target fiducial volume.

The target fiducial volume at each momentum was determined from a study of the distribution of reconstructed vertices. This resulted in the choice of a cylindrical effective target with a diameter at least $\frac{1}{2}$ in. smaller than that of the actual physical target. The actual target length was 12 in. (including hemispherical end caps) but the upstream end could not be seen by much of the system because of a brass target-mounting structure surrounding this portion of the target. The effective target length was taken to be 8.5 in., extending from +5.0 to −3.5 in. from the target center, with the positive sense being downstream.

The c.m. scattering angle for each event was de-

termined from the laboratory angle of the particle in the F arm of the apparatus. Each event satisfying the various cuts was weighted by the factor 1/(detection efficiency) for that particular c.m. scattering angle.

C. Kinematic Restrictions and Background Subtraction

The final steps in the analysis consisted of binning the reconstructed events, applying the kinematic cuts and manually subtracting the background events from each bin.

Since no magnets were used in the experiment, the remainder of the analysis depended upon the two available kinematic constraints. These are the coplanarity, $\hat{P}_b \cdot (\hat{P}_F \times \hat{P}_S)$, and the opening-angle deviation from elastic-scattering kinematics, $\theta_{S,\mathrm{lab}}^{\mathrm{measured}} - \theta_{S,\mathrm{lab}}^{\mathrm{kinematic}}$. Here $\hat{P}_b$, $\hat{P}_F$, and $\hat{P}_S$ represent unit vectors in the direction of the beam, the fast protons, and the slow protons, respectively. $\theta_{S,\mathrm{lab}}^{\mathrm{measured}}$ is the slow-proton laboratory angle as determined in the reconstruction and $\theta_{S,\mathrm{lab}}^{\mathrm{kinematic}}$ is the slow-proton laboratory angle predicted by using elastic-scattering kinematics and the measured laboratory angle of the fast proton.

First, all of the reconstructed events at a particular momentum were subjected to a 3-standard-deviation coplanarity cut. Figure 2 shows the coplanarity distribution for all events at 3.0 GeV/c which satisfy the fiducial volume cuts.

The remaining events were sorted into the appropriate 2° bins in $\theta_{\mathrm{c.m.}}$. For each bin, the distribution in the angular deviation from elastic-scattering kinematics was obtained. Figure 3 shows a typical opening-angle distribution at 3.0 GeV/c.

These histograms were used to determine the background level, by extrapolating the tails (from approximately ±1.5 times the FWHM) under the elastic peak. The resulting background subtraction at the lower momenta was typically less than

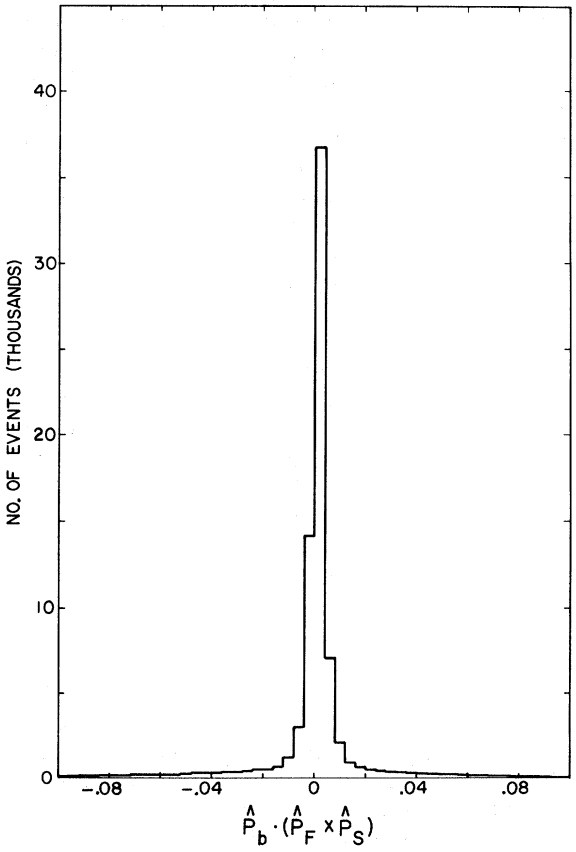

FIG. 2. Coplanarity distribution for all reconstructed events at 3.00 GeV/c. $\hat{P}_b$, $\hat{P}_F$, and $\hat{P}_S$ are unit vectors in the direction of the particles that enter the beam, fast-proton, and slow-proton detection arms, respectively.

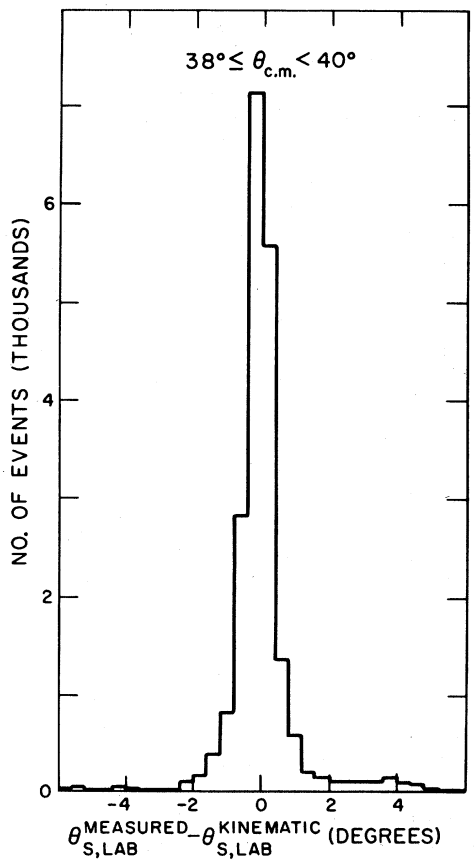

FIG. 3. Opening-angle distribution for all reconstructed events at 3.00 GeV/c with $38° \leq \theta_{\mathrm{c.m.}} \leq 40°$. $\theta_{S,\mathrm{lab}}^{\mathrm{measured}}$ is the measured scattering angle for the particle that enters the slow-proton detection arm. $\theta_{S,\mathrm{lab}}^{\mathrm{kinematic}}$ is the corresponding angle predicted by elastic-scattering kinematics on the basis of the measured scattering angle of the particle that enters the fast-proton detection arm.

5%, increasing to a maximum of about 10% at 3.5 GeV/c and to nearly 50% at very large angles at 5.5 GeV/c.

The remaining events were then used in calculating the differential cross section for each bin from

$$\frac{d\sigma}{d\Omega} = F\frac{N_w}{B\Delta\Omega},$$

where N_w is the weighted number of events in that bin, B is the total number of beam protons ($B_1B_2\bar{A}_H\bar{C}_G$ accumulated) at the particular momentum, $\Delta\Omega$ is the solid-angle element ($4\pi\sin\theta_{\text{c.m.}}/57.296$ for a 2° c.m. bin centered at $\theta_{\text{c.m.}}$), and where

$$F = 10^{30}\frac{1}{A_0\rho L_T},$$

A_0 being Avogadro's number, ρ the density of liquid hydrogen (0.07 g/cm^3), and L_T the effective target length in cm. This yields the differential cross section in μb/sr.

D. Corrections to the Data

Discussed briefly below are the various corrections which have been applied to the data. Where appropriate, the angular dependence of the corrections has been taken into account.

1. *Counter Inefficiencies*

The efficiency of each counter was measured by placing it in a beam defined by $B_1B_2\bar{A}_H$, and determining the ratio of counting rates

$$\frac{B_1B_2\bar{A}_HC_i}{B_1B_2\bar{A}_H}\,10^2,$$

which gives the percent efficiency of the counter C_i. On the basis of these measurements, all cross sections have been scaled up by 1% (±1%).

2. *Incident-Beam Absorption*

The recorded beam intensity ($B_1B_2\bar{A}_H\bar{C}_G$) denotes the proton flux at the upstream end of the target. Owing to absorption, the intensity of the beam as a function of position in the target is

$$I = I_0e^{-x/L_c},$$

where I_0 is the incident intensity ($B_1B_2\bar{A}_H\bar{C}_G$), x is the distance from the upstream end of the target, and L_c is the interaction length. Since $L_c \gg 12$ in., the maximum dimension of the target, a constant (energy-dependent) correction has been applied.

In the same manner, a constant correction has been made for beam absorption in counter B_2 and in the 0.010-in.-thick Mylar window of the target through which the beam passed.

These three corrections total about 3.8%.

3. *Nuclear Interaction of the Final-State Protons*

Each scattered proton, in reaching the F and S counters in order to produce a trigger, passed through liquid hydrogen in the target, four wire spark chambers, and the surrounding air. In each chamber the particles traversed a total of 0.010 in. of Mylar, 0.004 in. of Aclar, an average thickness of stainless steel (the wire mesh) of approximately 0.001 in., and an average thickness of copper (the wires in the chambers) of about 0.001 in. All of these thicknesses depend upon the scattering angle, which has been suitably taken into account for each $\theta_{\text{c.m.}}$ bin.

The resulting correction was typically 4.5% for the F arm and 1.8% for the S arm.

4. *Beam Contamination*

Corrections have been applied to the data to account for beam contamination arising from kaons, pions, and leptons, which escape the Čerenkov veto. The correction corresponding to the kaon component in the beam was determined to be approximately 2%. A correction of 0.3% was applied to account for the inefficiency of the Čerenkov counter in vetoing pions and leptons in the beam.

5. *Accidentals*

A 1% correction has been applied to the data to account for accidental counts due to chance satisfaction of beam logic requirements, and for chance anticounter vetoing of acceptable scatters.

6. *Reconstruction and Chamber Inefficiency*

In addition to loss of elastic scatters due to chamber inefficiency, there is some loss due to inability to obtain a proper reconstruction of events. This is most serious in the case where one of the final-state particle trajectories is determined by one of the two pairs of chambers which are closely spaced. The inherent scatter of sparks about the actual particle trajectory in this case could have the effects of producing a vertex located outside the target and subsequent loss of the event when the target cuts are applied. A correction of 2% has been applied to correct for this loss. This value was arrived at by carefully studying a large class of such events.

The individual chamber efficiencies initially measured were found to be consistent with system efficiency values arrived at by analyzing samples of the data with individual chambers or parts of chambers artificially eliminated. The system efficiency was determined to be approximately 98%, indicating a 2% correction.

TABLE I. Measured values of the differential cross section in p-p elastic scattering between 1.5 and 5.5 GeV/c. The errors given represent only the statistical uncertainty. In addition there is a ±7% normalization uncertainty.

$\theta_{c.m.}$ (deg)	$d\sigma/d\Omega$ (μb/sr)	Error (%)	$\theta_{c.m.}$ (deg)	$d\sigma/d\Omega$ (μb/sr)	Error (%)	$\theta_{c.m.}$ (deg)	$d\sigma/d\Omega$ (μb/sr)	Error (%)	$\theta_{c.m.}$ (deg)	$d\sigma/d\Omega$ (μb/sr)	Error (%)	$\theta_{c.m.}$ (deg)	$d\sigma/d\Omega$ (μb/sr)	Error (%)	$\theta_{c.m.}$ (deg)	$d\sigma/d\Omega$ (μb/sr)	Error (%)	$\theta_{c.m.}$ (deg)	$d\sigma/d\Omega$ (μb/sr)	Error (%)
P_L = 1.50 GeV/c			P_L = 1.65 GeV/c			P_L = 1.80 GeV/c			P_L = 2.00 GeV/c			P_L = 2.25 GeV/c			P_L = 2.50 GeV/c			P_L = 2.70 GeV/c		
47.64	4738	1.96	43.66	5179	1.88	39.67	5705	1.92	37.70	6094	3.66	31.73	7270	2.04	31.75	6424	1.92	31.77	5354	1.91
49.64	4211	2.03	45.65	4544	1.95	41.67	5157	1.96	39.69	4676	3.97	33.72	6179	2.14	33.75	5047	2.10	33.76	4434	2.03
51.63	3645	2.13	47.65	4097	2.01	43.67	4368	2.05	41.69	4193	4.07	35.72	5659	2.16	35.74	4352	2.19	35.76	3526	2.20
53.63	3488	2.12	49.65	3611	2.07	45.67	3725	2.16	43.68	3789	4.24	37.72	4645	2.31	37.74	3492	2.36	37.76	2837	2.37
55.63	3277	2.14	51.64	3160	2.17	47.66	3499	2.18	45.68	3081	4.45	39.71	3831	2.46	39.73	2979	2.47	39.75	2304	2.56
57.63	2854	2.25	53.64	2879	2.24	49.66	3076	2.27	47.68	2563	4.77	41.71	3386	2.53	41.73	2462	2.66	41.75	1779	2.83
59.62	2641	2.30	55.64	2411	2.42	51.66	2719	2.34	49.67	2277	2.68	43.71	2813	2.68	43.73	1925	2.92	43.74	1532	2.98
61.62	2421	2.35	57.63	2208	2.46	53.65	2331	2.50	51.67	1906	2.90	45.70	2326	2.88	45.72	1634	3.09	45.74	1214	3.24
63.62	2152	2.44	59.63	2081	2.48	55.65	2110	2.57	53.67	1610	3.11	47.70	1863	3.13	47.72	1362	3.30	47.73	940.8	3.64
65.61	2057	2.45	61.63	1885	2.55	57.64	1876	2.69	55.66	1453	3.19	49.69	1560	3.30	49.71	1185	3.42	49.73	822.9	3.74
67.61	1872	2.52	63.62	1691	2.66	59.64	1683	2.76	57.66	1334	2.51	51.69	1412	3.39	51.71	977.4	3.71	51.72	646.2	4.30
69.61	1678	2.64	65.62	1471	2.76	61.64	1438	2.91	59.65	1146	2.68	53.68	1115	3.79	53.70	834.9	3.93	53.72	610.5	4.23
71.60	1510	2.74	67.62	1351	2.86	63.63	1307	3.01	61.65	1037	2.74	55.68	991.7	3.93	55.70	705.1	4.21	55.71	511.5	4.48
73.60	1383	2.82	69.61	1163	3.03	65.63	1155	3.15	63.64	945.0	2.81	57.67	875.9	3.11	57.69	613.6	4.44	57.70	472.8	4.64
75.60	1350	2.81	71.61	1097	3.07	67.62	1040	3.24	65.64	833.2	2.92	59.67	774.6	3.22	59.69	565.6	3.33	59.70	399.4	4.85
77.59	1225	2.91	73.61	1040	3.10	69.62	955.1	3.37	67.64	763.9	3.02	61.66	707.9	3.31	61.68	480.7	3.63	61.69	366.7	3.89
79.59	1068	3.00	75.60	923.1	3.23	71.62	903.9	3.41	69.63	730.4	3.04	63.66	656.1	3.35	63.67	466.0	3.62	63.69	363.7	3.78
81.58	1097	2.80	77.60	856.3	3.27	73.61	788.4	3.63	71.63	612.7	3.30	65.65	562.4	3.60	65.67	405.8	3.91	65.68	313.4	3.98
83.58	1033	2.74	79.59	797.0	3.18	75.61	762.6	3.59	73.62	617.4	3.19	67.65	557.7	3.44	67.66	381.9	3.84	67.67	317.3	3.98
85.58	1025	2.61	81.59	802.5	3.02	77.60	689.7	3.51	75.62	578.3	3.13	69.64	470.3	3.72	69.66	361.9	3.87	69.67	287.2	4.14
87.57	1009	2.52	83.59	765.4	2.92	79.60	639.8	3.45	77.61	560.3	2.99	71.64	434.3	3.88	71.65	347.9	3.81	71.66	275.3	3.97
89.57	1017	2.43	85.58	713.9	2.88	81.59	623.1	3.31	79.61	539.8	2.84	73.63	405.7	3.70	73.64	336.9	3.56	73.65	258.9	3.71
			87.58	720.9	2.76	83.59	594.1	3.23	81.60	518.5	2.75	75.63	398.8	3.50	75.64	321.6	3.35	75.65	248.8	3.42
			89.57	655.5	2.88	85.59	569.4	3.15	83.60	489.8	2.70	77.62	375.8	3.38	77.63	302.4	3.29	77.64	260.1	3.19
						87.58	600.6	3.02	85.59	466.7	2.68	79.62	362.3	3.22	79.62	302.8	3.14	79.63	237.1	3.16
						89.58	564.5	3.07	87.59	459.2	2.70	81.61	354.8	3.12	81.62	297.4	3.08	81.63	230.9	3.16
									89.58	465.0	2.69	83.60	371.6	2.96	83.62	286.7	3.09	83.62	220.6	3.19
												85.60	354.7	3.01	85.61	286.6	3.07	85.61	236.0	3.06
												87.59	336.8	3.09	87.60	266.4	3.16	87.60	214.8	3.19
												89.59	342.1	3.05	89.59	284.0	3.05	89.60	221.5	3.17

TABLE I *(Continued)*

$\theta_{c.m.}$ (deg)	$d\sigma/d\Omega$ (μb/sr)	Error (%)	$\theta_{c.m.}$ (deg)	$d\sigma/d\Omega$ (μb/sr)	Error (%)	$\theta_{c.m.}$ (deg)	$d\sigma/d\Omega$ (μb/sr)	Error (%)	$\theta_{c.m.}$ (deg)	$d\sigma/d\Omega$ (μb/sr)	Error (%)	$\theta_{c.m.}$ (deg)	$d\sigma/d\Omega$ (μb/sr)	Error (%)	$\theta_{c.m.}$ (deg)	$d\sigma/d\Omega$ (μb/sr)	Error (%)
P_L = 3.00 GeV/c			P_L = 3.50 GeV/c			P_L = 4.00 GeV/c			P_L = 4.50 GeV/c			P_L = 5.00 GeV/c			P_L = 5.50 GeV/c		
31.79	4482	1.77	31.84	3201	1.93	31.88	2257	1.75	31.91	1543	2.02	31.95	1058	3.00	31.99	684.3	2.05
33.79	3546	1.95	33.83	2375	2.16	33.87	1671	1.97	33.91	1085	2.38	33.95	731.8	3.49	33.98	452.8	2.40
35.78	2848	2.10	35.82	1837	2.38	35.86	1192	2.22	35.90	798.2	2.60	35.94	521.7	3.96	35.97	309.5	2.79
37.78	2196	2.27	37.82	1406	2.64	37.86	841.1	2.61	37.90	569.3	3.03	37.93	341.7	4.81	37.97	215.7	3.24
39.77	1770	2.43	39.81	1046	3.00	39.85	653.7	2.84	39.89	418.7	3.36	39.92	252.8	5.32	39.96	155.1	3.69
41.77	1323	2.73	41.81	830.2	3.21	41.85	516.6	3.14	41.88	301.1	3.82	41.92	202.1	6.06	41.95	123.4	4.08
43.77	1037	3.02	43.80	664.8	3.51	43.84	403.1	3.45	43.87	245.0	4.12	43.91	162.9	6.51	43.94	95.63	4.58
45.76	816.3	3.38	45.80	507.9	4.02	45.83	320.6	3.76	45.87	201.6	4.52	45.90	117.1	7.54	45.93	73.04	5.16
47.75	713.7	3.47	47.79	457.2	4.01	47.82	265.2	4.00	47.86	168.6	4.74	47.89	94.25	8.08	47.92	53.54	6.11
49.75	586.3	3.73	49.78	366.2	4.32	49.82	235.6	4.17	49.85	143.3	4.97	49.88	73.66	8.70	49.91	40.49	6.49
51.74	520.1	3.84	51.78	296.1	4.75	51.81	189.8	4.60	51.84	120.7	5.28	51.87	61.86	9.80	51.90	34.20	6.91
53.74	421.0	4.16	53.77	267.3	4.97	53.80	171.6	4.90	53.83	98.64	6.04	53.86	53.37	9.90	53.89	25.27	8.28
55.73	385.7	4.20	55.76	232.1	5.15	55.79	132.0	5.33	55.82	75.13	6.48	55.85	39.73	11.29	55.88	25.01	8.44
57.72	360.7	4.32	57.75	221.7	5.31	57.79	124.9	5.31	57.81	71.35	6.65	57.84	36.12	12.17	57.87	19.68	9.48
59.72	331.4	4.42	59.75	198.4	5.35	59.78	107.5	5.74	59.81	58.30	7.14	59.83	30.04	12.69	59.86	14.93	10.23
61.71	294.4	4.64	61.74	167.7	5.82	61.77	91.65	6.19	61.80	51.94	7.88	61.82	22.67	15.11	61.85	13.74	11.17
63.70	274.2	3.58	63.73	145.3	6.46	63.76	77.68	6.37	63.79	43.95	8.06	63.81	21.59	15.81	63.84	12.10	11.57
65.70	247.2	3.71	65.72	124.9	6.71	65.75	72.69	6.62	65.78	36.62	8.68	65.80	15.73	16.78	65.83	10.95	12.14
67.69	219.5	3.87	67.72	124.3	4.64	67.74	64.18	7.26	67.77	31.80	9.22	67.79	14.65	16.84	67.81	7.533	14.17
69.68	217.1	3.81	69.71	113.3	4.89	69.73	53.76	5.36	69.76	30.19	10.75	69.78	13.68	17.76	69.80	7.295	15.83
71.67	209.2	3.69	71.70	99.69	4.96	71.72	45.67	5.53	71.75	25.76	7.90	71.77	12.47	18.98	71.79	9.582	14.56
73.67	198.4	3.38	73.69	91.43	4.71	73.71	41.11	5.55	73.73	25.64	8.23	73.76	12.65	14.57	73.78	7.195	18.04
75.66	189.0	3.07	75.68	83.04	4.41	75.70	38.21	5.33	75.72	22.59	8.67	75.75	12.06	16.71	75.77	6.285	20.84
77.65	185.1	2.94	77.67	81.04	4.32	77.69	35.02	5.41	77.71	19.11	9.36	77.73	10.55	15.44	77.75	6.869	19.00
79.64	177.8	2.99	79.66	81.54	4.16	79.68	34.34	4.98	79.70	19.57	8.23	79.72	9.689	14.14	79.74	6.164	18.82
81.64	168.8	3.01	81.66	76.02	4.33	81.67	32.06	5.10	81.69	18.42	8.75	81.71	10.10	16.15	81.73	5.799	17.94
83.63	168.2	3.03	83.65	75.51	4.32	83.66	32.71	4.81	83.68	17.31	7.52	83.70	11.54	12.70	83.71	4.880	20.33
85.62	166.0	3.02	85.64	74.77	4.16	85.65	30.84	5.04	85.67	16.56	7.37	85.69	9.821	13.80	85.70	4.553	17.76
87.61	161.0	3.05	87.63	68.21	4.81	87.64	27.81	5.24	87.66	17.69	6.68	87.67	9.926	11.99	87.69	4.680	15.52
89.61	149.6	4.24	89.62	69.16	4.23	89.63	29.37	5.03	89.65	17.19	7.03	89.66	9.234	13.50	89.68	5.350	13.24

7. *Target-Empty Background*

Numerous target-empty runs were made during the experiment and the resulting data were subjected to the standard analysis. The target-empty events can be explained as originating from scatters in the walls of the hydrogen target vessel and from scatters in the residual hydrogen gas in the target. The beam spot size and the spatial cuts on the interaction vertex were such that target-empty corrections to the data were unnecessary.

E. Checks

Several methods have been used to determine the internal consistency of the method of analysis and of the resulting data.

One procedure was frequently used to check the fiducial volume of the detection system. This consisted of subjecting the recorded events to the usual reconstruction, and then histogramming the horizontal and vertical coordinates of the point of intersection of the reconstructed trajectory with the planes of the F- and S-counter arrays. In this manner, the location of the edges of the counters (outside which no intersections would occur ideally) were accurately verified.

Two methods were used to investigate the manual background-subtraction procedure and consistency. The first was to reverse the order of applying the kinematic constraints by imposing the opening-angle cut on the data prior to binning, and then making the manual background subtractions on the coplanarity distributions of the binned events. At the lower energies, the two methods gave very consistent results. Above 3.5 GeV/c however, the latter method proved superior, since the opening-angle distributions in some bins were asymmetric, making an accurate background subtraction more difficult. This was due to these bins falling close to the scintillation-counter edges. The coplanarity distributions were symmetric, however, and in these cases the final background was determined from the coplanarity distributions.

The second method used to check the background subtraction involved investigating the coplanarity (opening angle) of the events lying outside the opening-angle (coplanarity) cut used in determining the background level. Peaking of these distributions would have indicated the possibility of having elastic events not included in the corresponding cut.

IV. RESULTS

The differential cross sections are presented in Table I for the 13 incident proton momenta of this experiment. The quoted errors include only the combined statistical uncertainties in the signal (S) and background (B) as calculated from

$$\frac{\Delta(d\sigma/d\Omega)}{d\sigma/d\Omega} = \frac{(S+2B)^{1/2}}{S} .$$

There is also a normalization uncertainty of ±7% in the data. This is due primarily to the uncertainty in the corrections which have been applied to the data.

The results are shown graphically in Fig. 4. The lines drawn through the data are hand-drawn fits, intended to guide the eye. The angular distribution at each energy is quite smooth. We observe no strong evidence for secondary diffraction-like be-

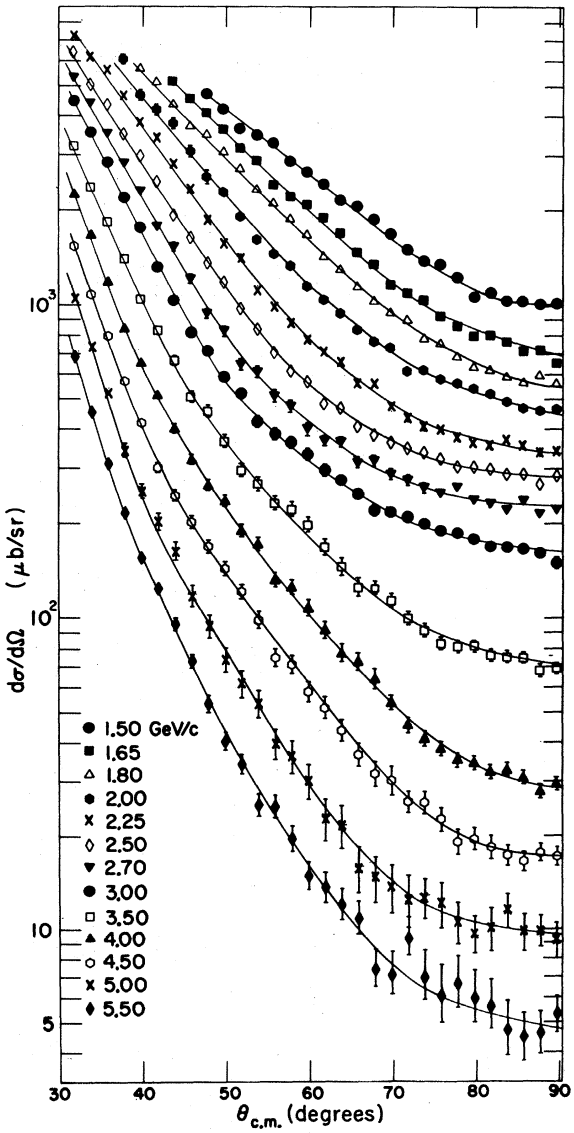

FIG. 4. Differential cross sections for p-p elastic scattering between 1.5 and 5.5 GeV/c measured in the present experiment. The smooth lines shown are hand-drawn fits to the data.

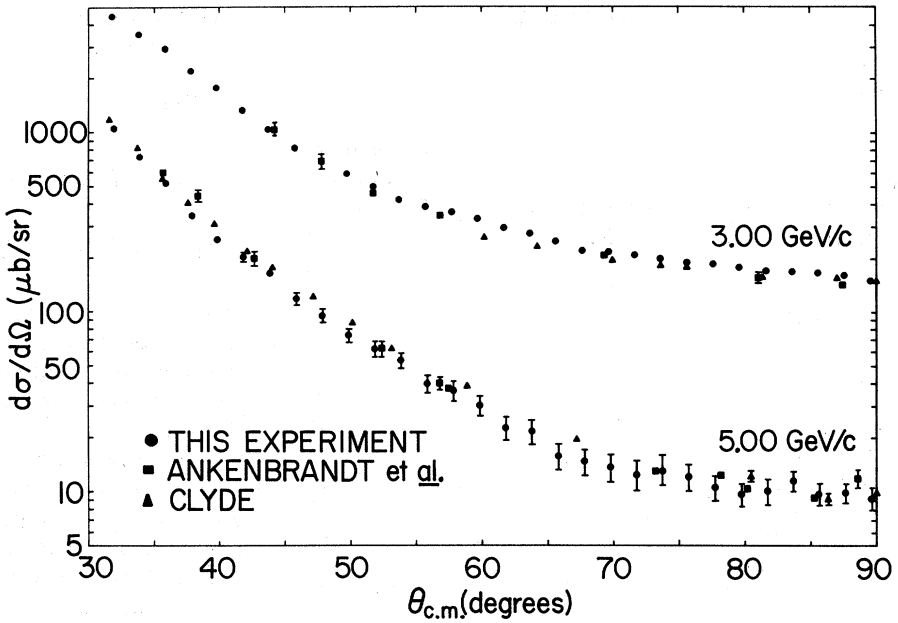

FIG. 5. Comparison of data from this experiment at 3.0 and 5.0 GeV/c with those of Clyde (Ref. 10) and Ankenbrandt *et al.* (Ref. 11).

havior as seen by Allaby *et al.*[6] at higher momenta. The angular distribution at each energy is roughly linear on this plot from $\theta_{c.m.} = 30°$, where these data begin, to a c.m. angle corresponding to a constant value of $-t \approx 0.7$ (GeV/c)^2, where structure in the polarization is observed. Beyond this angle, the distribution smoothly begins to flatten and approach 90° with a slope consistent with zero as required by the Pauli principle.

Figure 5 presents a comparison of our data at 3.0 and 5.0 GeV/c with those from two earlier experiments of Clyde[10] and Ankenbrandt *et al.*[11] This agreement is, in general, within the combined statistical and normalization uncertainties. However, a systematic discrepancy appears to exist between the data from this experiment and those of Clyde at 3.0 GeV/c near 60° in the c.m. We observe a slight shoulder [at about $-t = 1$ (GeV/c)^2] reminiscent of the structure observed by Allaby *et al.*[6] in this region while Clyde's data remain relatively flat from 90° to an unusually small angle at this momentum.

The differential cross section at 90° as a function of $-t$ is presented in Fig. 6. This figure summarizes most of the existing 90° data between $-t = 0.5$ and $-t = 10$ (GeV/c)^2. We show a break observed by Akerlof *et al.*[8] near $-t = 6.5$ (GeV/c)^2. The dashed line drawn through the low-energy data[11] is a hand-drawn fit. As shown, our data are quite consistent with Akerlof *et al.*[8] at 5.0 and 5.5 GeV/c, and with the low-energy data at 1.5 and 1.65 GeV/c. Our data indicate that the suspected break at small $-t$ occurs quite close to $-t = 0.8$ (GeV/c)^2. In addition, we observe another less pronounced slope change near $-t = 3$ (GeV/c)^2.

The three solid lines appearing in Fig. 6 have resulted from linear regression fits to the data. In each of the three regions, the fit results in an average value of χ^2 per datum point of about 1, while a fit to the data for $0.8 \leq -t \leq 6$ (GeV/c)^2 with a single exponential in $-t$ results in a significantly poorer χ^2 per datum point of 13.

The existence of the break near $-t = 3$ (GeV/c)^2 had been graphically implied by Allaby *et al.*[6] some time ago. In Ref. 6, they presented a plot of $d\sigma/dt$ vs $-t$ with points of constant $\theta_{c.m.} = 90°$, 80°, and 60° connected, respectively, by straight lines. They observed that the 90° break at $t \approx -6.5$ (GeV/c)^2 was apparent at the other angles. They also showed a break near $-t = 3$ (GeV/c)^2 for the $\theta_{c.m.} = 60°$ and 80° data. The situation near this t value is shown in more detail in Fig. 7. Here we have plotted data from the CERN experiments (Ref. 7), Akerlof *et al.*,[8] Clyde,[10] Ankenbrandt *et al.*,[11] and some of the data from this experiment. Points of constant $\theta_{c.m.} = 90°$, 80°, and 70° are connected. As shown, a change in slope occurs near $t = -3$ (GeV/c)^2 regardless of the angle.

V. INTERPRETATION

We have attempted to interpret the results of this experiment in terms of several models. In so doing, it was hoped that the detailed angular distribution data would be sufficiently restrictive so as to allow some physical interpretation of the structure observed in the data, notably the breaks in the 90° cross section.

The results of these attempts are described below.

A. Optical Models

We have compared the predictions of the classical optical model of Fernbach *et al.*[13] with the results of the experiment. This model was initially proposed to describe the scattering of high-energy neutrons from nuclei but has been applied to high-energy particle scattering phenomena. (See, for example, Refs. 14 and 15.)

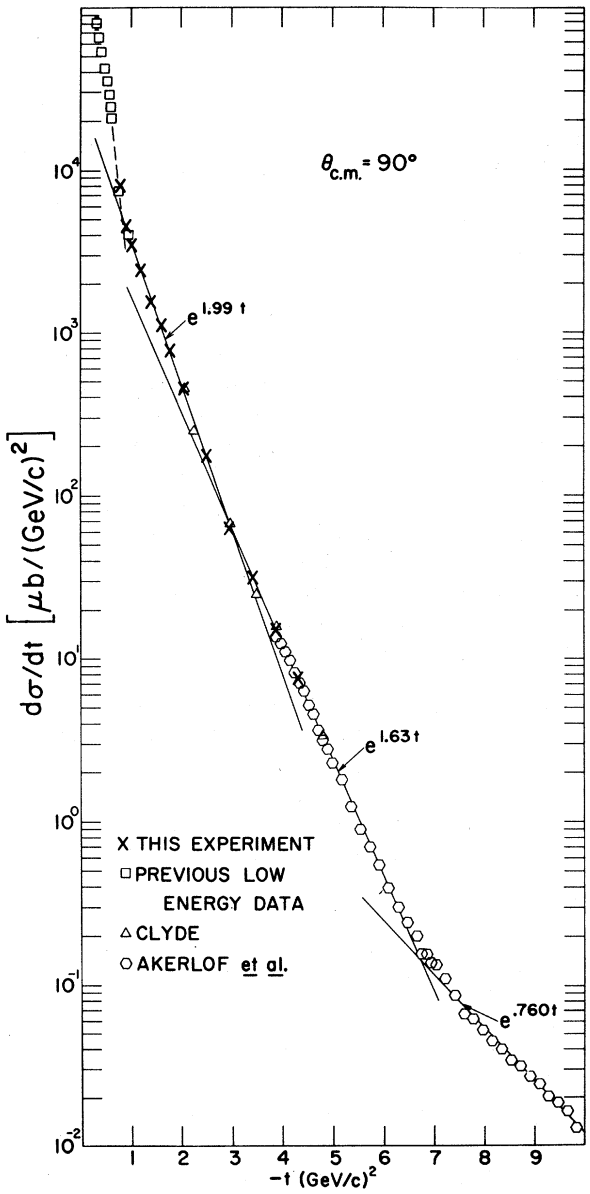

FIG. 6. Differential cross section in p-$\bar{p}$ elastic scattering at $\theta_{c.m.} = 90°$. The low-energy data shown as open squares are taken from Ref. 12. The open triangles represent data from Clyde (Ref. 10), and the open hexagons represent data from Akerlof *et al.* (Ref. 8).

The scattering amplitude, elastic cross section, and absorption cross section are given by

$$f(\theta) = K \int_0^\infty (1 - ae^{i\varphi}) J_0(Kb \sin\theta) b \, db,$$

$$\sigma_{el} = 2\pi \int_0^\infty |1 - ae^{i\varphi}|^2 b \, db,$$

$$\sigma_{ab} = 2\pi \int_0^\infty (1 - a^2) b \, db,$$

where $\theta_{c.m.}$ is the scattering angle, b is the impact parameter, K is the c.m. momentum, and a and φ are the amplitude and phase shift of the scattered wave corresponding to an incident wave of unit amplitude and zero phase shift. Proton spin effects are neglected. Following the approach of Cork *et al.*[14] we have further limited the model to correspond to (a) a purely absorbing disk, $\varphi = 0$, $a = a_1$, for $0 \leq b \leq R$, and $\varphi = 0$, $a = 1$, for $b > R$; (b) an absorbing disk with short-range phase shift, $\varphi = C_1$, $a = a_1$, for $0 \leq b \leq R_1$, $\varphi = 0$, $a = a_2$, for $R_1 \leq b \leq R_2$; and finally, (c) a tapered absorbing disk with short-range phase shift, $a = 1 - A[1 - (b/R_2)^2]$ with A and φ being constant within each of two spherical regions defined by radii R_1 and R_2 as above.

The purely absorbing disk gave acceptable fits to the data only at 1.5 GeV/c with $R \approx 0.9$ F. Above this, two regions (model b) were required. Good fits were obtained between 1.65 and 3.00 GeV/c to the angular distribution, and the elastic and absorption cross sections with $R_1 = 0.6$ F and $R_2 = 1.2$ F. Above 3.0 GeV/c, the model began to exhibit structure not present in the data. This structure took the form of a dip which appeared at large angles. This is characteristic of models with sharp cutoffs. Tapering of the edges, as in model c, eliminates this objectionable behavior. Using model c, the fits were extended to higher momenta. As an example of the results obtained with model c, the fits at 1.50 and 2.70 GeV/c are shown in Fig. 8. In order to fit the data at all energies, it was required that the radii be allowed to vary in the range $0.5 \lesssim R_1 \lesssim 0.9$ F and $1.1 \lesssim R_2 \lesssim 1.5$ F.

The results described above are quite consistent with those of Cork *et al.*[14] One of the more objectionable features of this type of model is that it is necessary to allow the radii to vary in fitting data over a sizable energy range. We have tried to extend these models in order to remove this objection. Our first attempt was to modify model b by adding an additional region. This resulted in good fits at all energies, but uniqueness problems arose and, at 5.0 and 5.5 GeV/c, unwanted structure again began to appear due to the sharp cutoff.

The second attempt consisted of trying to get one step closer to reality by introducing a single spin-flip amplitude into model b. This was of the form

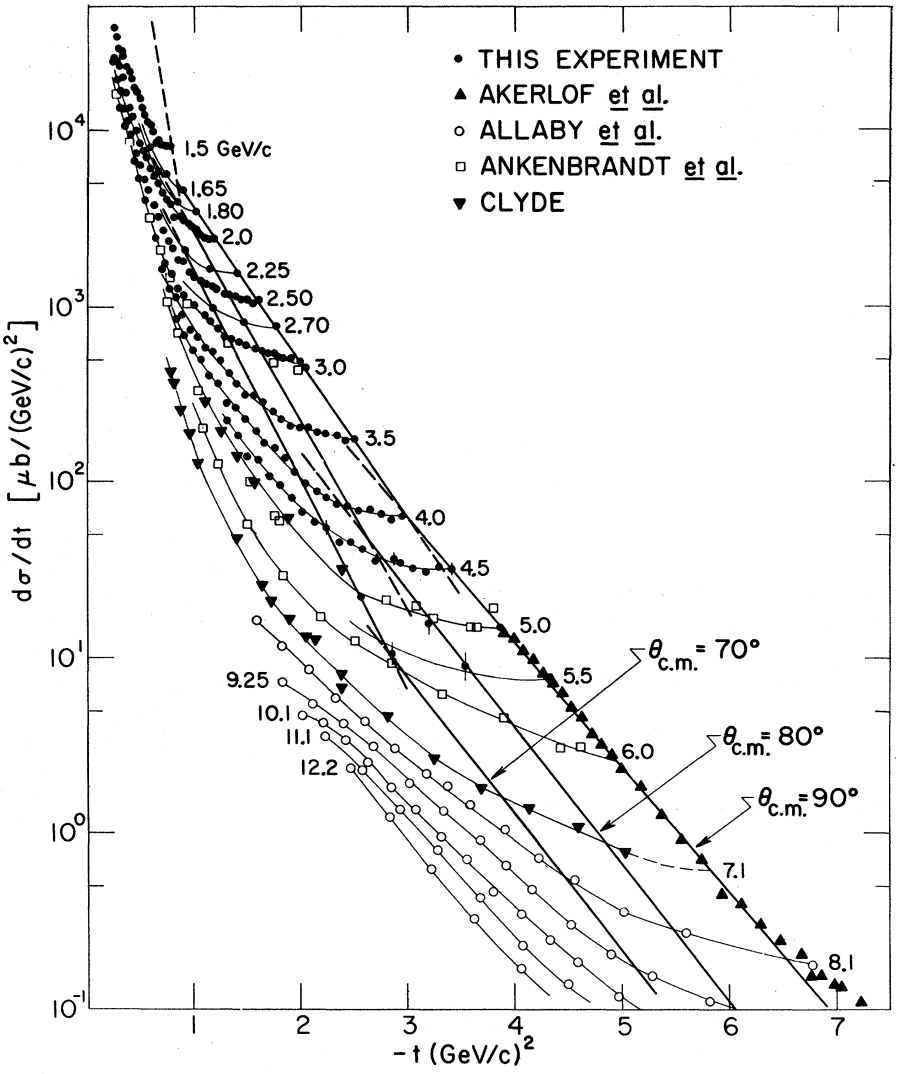

FIG. 7. Differential cross sections in p-p elastic scattering at fixed values of $\theta_{c.m.}$. The data of Akerlof *et al.* are taken from Ref. 8, those of Allaby *et al.* from Ref. 7, those of Ankenbrandt *et al.* from Ref. 11, and those of Clyde from Ref. 10. The solid circles represent part of the data from the present experiment.

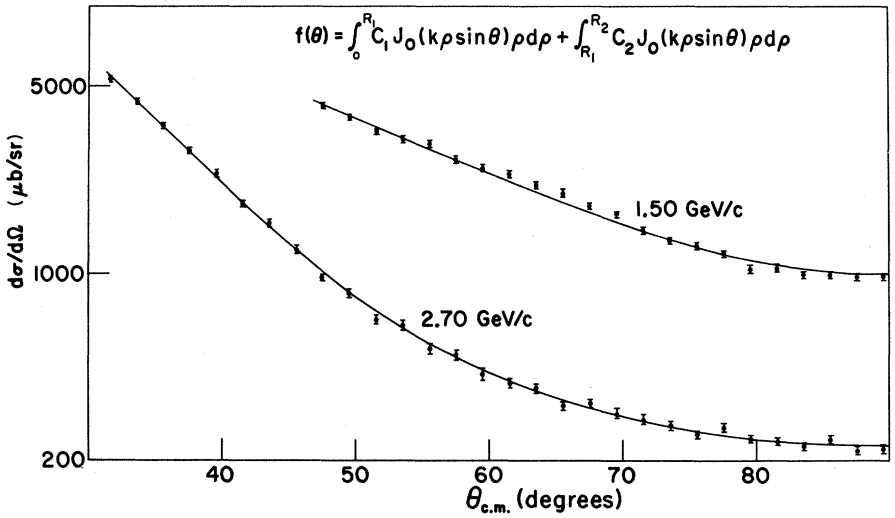

FIG. 8. Optical-model fits to the data at 1.50 and 2.70 GeV/c. C_1 and C_2 have been taken to be constant. At 1.50 GeV/c, R_1=0.5 F and R_2 =1.09 F. At 2.7 GeV/c R_1 =0.53 F and R_2=1.47 F.

suggested, in principle, by the hadronic form-factor approach of Durand and Lipes[16] in which weak L-S coupling gives rise to an analogous amplitude. The same parametrization was used as in model *b*. By adding this term it was hoped that we could fit not only the angular distribution and total cross section, but also the polarization. This was rather unsuccessful in that the angular distributions required a smaller spin-flip contribution than did the polarization.

Although these simple forms of the optical model are capable of providing reasonably good fits to the data (the angular distribution, total elastic cross section, and total absorption cross section) the physical interpretations of the results are, at best, nebulous due to the complex spin structure of the p-p system.

B. Krisch's Model

We have attempted to interpret our data in terms of a model due to Krisch[17-20] by investigating the differential cross section as a function of the proposed universal parameter $(\beta P_\perp)^2$,

$$\frac{d\sigma}{d\Omega}=\sum_{i=1}^{3}A_i e^{-a_i(\beta P_\perp)^2},$$

where the three terms correspond to three separate regions of the spatial volume in which the particles collide, and $P_\perp = P\sin\theta_{\text{c.m.}}$.

This parametrization is intended to remove the energy dependence of the differential cross section.

As pointed out in Ref. 7, application of Krisch's model in its modified form,[20] when examined on a more revealing scale, was not totally satisfactory in removing the energy dependence in their data at higher momenta. The corresponding investigation at the lower momenta of the present experiment leads to a concordant conclusion. Figure 9 shows some of the data from this experiment, from Clyde[10] and from Ref. 7 plotted as a function of $(\beta P_\perp)^2$. The line appearing on this figure uses the parameters reported by Krisch[20] in fitting the data. We note the violent disagreement of our low-energy data with the proposed fit. At the higher momenta ($P_L \geq 4.0$ GeV/c) the agreement improves considerably but tends to oscillate somewhat about the line. This is similar to the results at very high momenta.

In conclusion, it should again be pointed out that at low momenta the angular distribution cannot be considered diffractive in nature and Krisch's model should not be expected to be valid. In his fits, Krisch placed the minimum momentum cutoff arbitrarily at 5.0 GeV/c.[20] The deviation of our low-energy data from the model is perhaps a manifes-

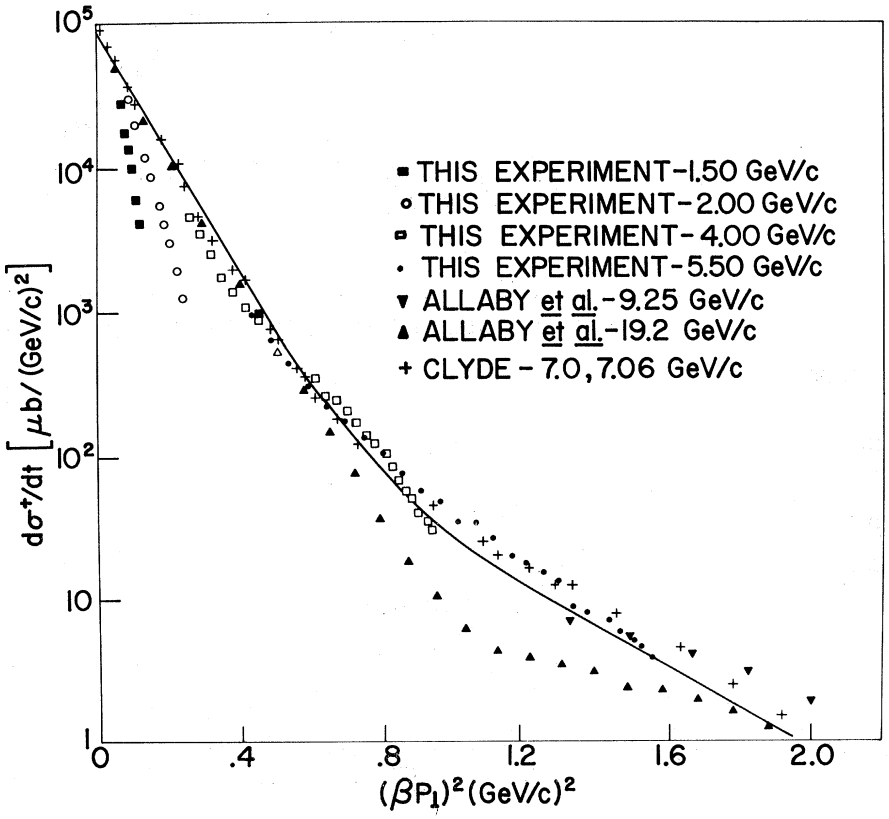

FIG. 9. $d\sigma^\dagger/dt$ as a function of $(\beta P_\perp)^2$, where β is the velocity of the protons in the c.m. system and $P_\perp$ is the transverse momentum. The solid triangles represent data from Ref. 7 and the crosses are data from Ref. 10. The relationship between $d\sigma^\dagger/dt$ and $d\sigma/dt$ is given in Ref. 20.

tation of the nondiffractive nature of the data.

C. Statistical Model

We have fitted an Orear-type function[21]

$$\frac{d\sigma}{d\Omega}=Ae^{-P_\perp/g},$$

which arises, for instance, from statistical and thermodynamic models,[22-24] to the large-angle data. A and g are free parameters.

Allaby *et al.*,[4] using this type of fit, noted that the observed marked change in the nature of the angular distribution near 8 GeV/c was reflected in a marked change in g, going from one constant value at lower momenta to another possibly constant value at higher momenta.

In fitting the data with this functional form there is some uncertainty in the meaning of the term "large-angle." For $80° \leq \theta_{c.m.} \leq 90°$, the differential cross section and $P_\perp$ are both nearly independent of angle, so that the parameter g is not well determined. The attitude taken in our application of the model was to assume that the data between 75° and 90° could be fit with this form. The fit was then extended to smaller angles, requiring that there be no significant changes in the parameters and that the quality of the fit be maintained (no serious degradation in the average χ^2 per data point). This typically resulted in fits to the data from near 60° to 90°.

The results of these fits are shown in Fig. 10 where g is plotted as a function of momentum. This figure includes our data together with that of other experiments.[7,10,11] Rapid changes in g are noted to appear near 1.5, 4.0, and as Allaby *et al.*[4] observed, 8.0 GeV/c. It should be noted that these momentum values closely correspond to the positions of the breaks in the 90° cross section shown in Sec. IV.

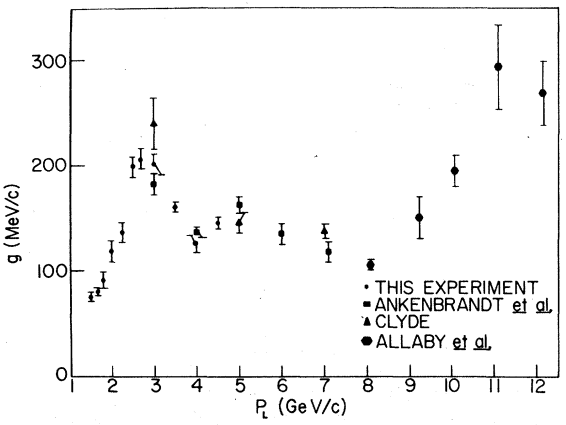

FIG. 10. The momentum dependence of the parameter g which occurs in the relation $d\sigma/d\Omega = Ae^{-P_\perp/g}$, where $P_\perp$ is the transverse proton momentum in the c.m. system. The solid squares refer to data from Ref. 11. The solid triangles refer to data from Ref. 10, and the solid hexagons to data from Ref. 7.

D. Effective Regge Trajectory

We have applied a simple Regge model to our data. Pinsky[25] has argued that high-energy p-p elastic scattering can be represented at large angles in the framework of the Regge-pole model with the cross section being given by

$$\frac{d\sigma}{d\Omega}=\frac{1}{s}K(t)\left(\frac{\nu}{s_0}\right)^{2\alpha(t)},$$

with

$$\nu=\tfrac{1}{2}(s-u)$$

and $K(t)$ containing the contribution of the residue and signature factor. One prediction of this relation is that if one makes a log-log plot of $d\sigma/d\Omega$ versus ν at a constant value of $-t$, a straight line with a slope of 2α should result. Pinsky[25] and Sacharidis[7] have shown this to be consistent with the CERN high-energy p-p scattering data.[4-7]

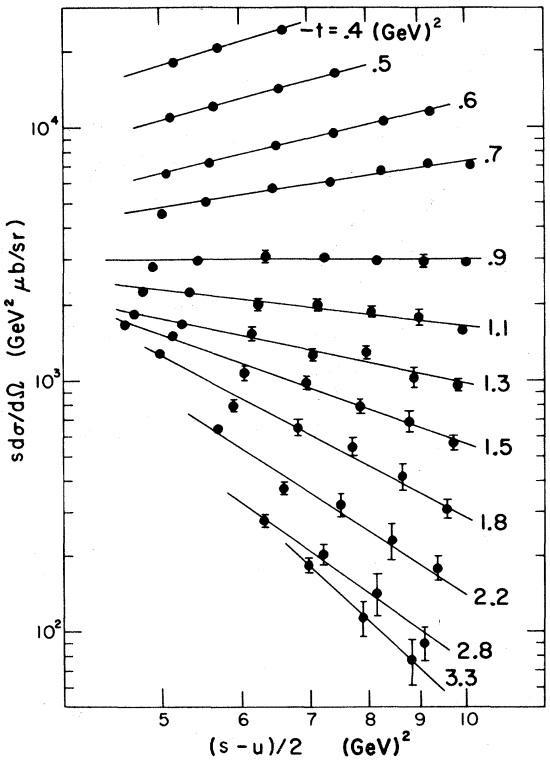

FIG. 11. Plot of log $(sd\sigma/d\Omega)$ against $\log\frac{1}{2}(s-u)$ based on data between 2.7 and 5.5 GeV/c from the present experiment. s and u are the Mandelstam variables.

In Fig. 11, we show the results of this approach as applied to our data ($P_L \geq 2.7$ GeV/c). Figure 12 is a comparison of our results with those of Ref. 7. Both sets of data are individually consistent with the prediction, but there is a significant difference in the slopes of the lines. In Fig. 13, we show the effective trajectories extracted from the two sets of data. The values of α_{eff} from the data of Allaby *et al.*[4-6] are those reported in Ref. 7. We observe that the characteristics of the two trajectories are somewhat similar, being linear in the small $-t$ region and flattening at large $-t$.

The linear region of the effective trajectory obtained from the data from this experiment [$0.7 \leq -t \leq 2$ (GeV/c)^2] has a slope of about 1.2 and an intercept of slightly more than one. It is interesting to note that if one extrapolates a straight-line fit to the small $-t$ region of α_{eff} derived from the higher-energy data, it is consistent with the α_{eff} from this experiment.

E. Breaks in the 90° Cross Section

The combination of the data from this experiment and that of Akerlof *et al.*[8] and cyclotron experiments[6] indicates the existence of three well-defined and rather rapid changes in slope of the 90° cross section at $-t \approx 0.8$, 3, and 6.5 (GeV/c)^2. These breaks should then be reflected in Krisch's plot[20] at $(\beta P_\perp)^2 \approx 0.12$, 0.95, and 2.6 (GeV/$c$)^2. The latter corresponds to one of the two discontinuities reported by Krisch.[20] However, only one of the two small $-t$ breaks has been accounted for in the model.

This is not an indication of an inconsistency, however, since the small $-t$ breaks in the 90° cross section occur at low momenta where Krisch's model is not expected to offer a description of the data.

The existence of a third discontinuity in the $\theta_{\text{c.m.}} = 90°$ cross section has been predicted by at least three models. Fleming *et al.*[26] have proposed a semiempirical model which was motivated by the successes of the Krisch model,[20] but which attempted to circumvent some of its theoretical difficulties (primarily its failure to satisfy the Cerulus-Martin bound[27]). In addition, this model asymptotically yields the Orear exponential behavior in $P_\perp$. Basically they propose that the sum of three exponentials in $(\beta P_\perp)^2$ suggested by Krisch[20] be replaced by an infinite sum of exponentials in the same parameter. The leading behavior of the cross section is still given by the Krisch-type equation. The result of this proposed model is the prediction of an infinite number of breaks, two of which are those predicted by Krisch, and another which is expected to occur near $t = -3$ (GeV/c)^2.

It has been suggested by Libby[28] that the interaction energy between colliding protons can be cal-

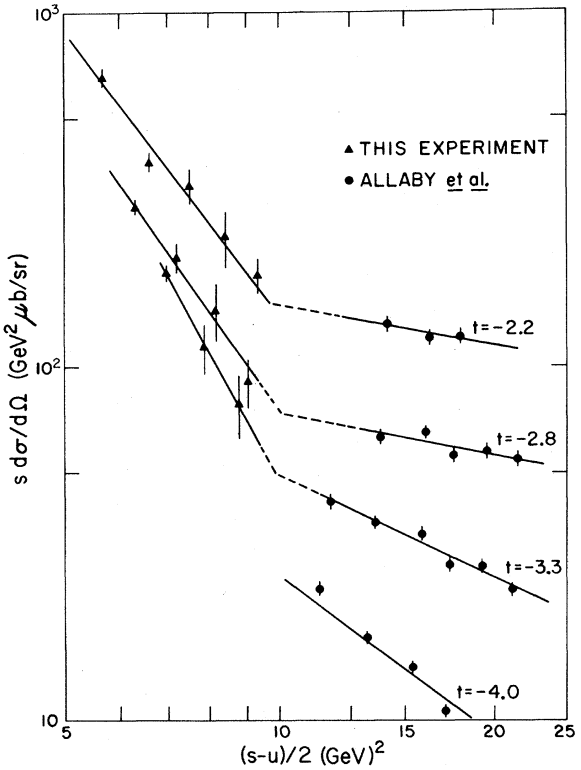

FIG. 12. Plot of log ($sd\sigma/d\Omega$) against log $\frac{1}{2}(s-u)$. The points shown as solid triangles are determined from data of the present experiment. The points shown as solid circles are determined from the higher-energy CERN data tabulated in Ref. 7.

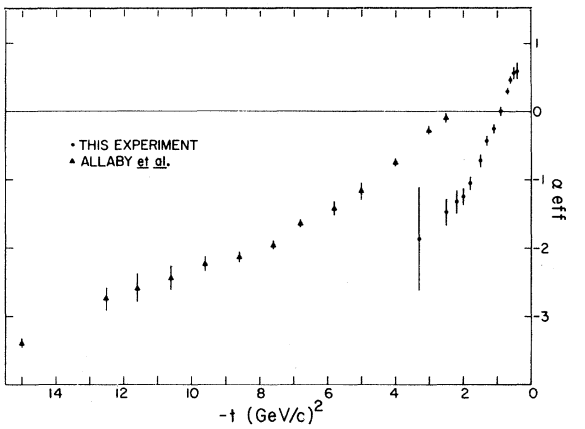

FIG. 13. Effective Regge trajectories for p-p elastic scattering at intermediate and high momenta. The points shown as solid circles are calculated from the data of the present experiment in the momentum region between 2.7 and 5.5 GeV/c. The points shown as solid triangles are calculated from the data of Ref. 7 which cover the momentum region between ~8 and 21 GeV/c.

culated from the high-energy differential cross-section data. The model gives a relationship between E (the interaction energy) and r (the nucleon separation). Depending upon the energy range of the data used in the computation, four E-versus-r curves result. The four wells obtained have different depths and different nucleon separations at the minimum interaction energy. It is suggested that these four wells, which correspond to the four linear sections of the fixed-angle cross section, belong to specific excited states of the two-baryon system.

The third model suggesting the existence of additional breaks is due to Libby and Predazzi.[29] They have presented a combination of experimental and theoretical evidence for the existence of a Regge trajectory for the two-baryon system. The result is the prediction of a small $-t$ break [$t \approx -0.8$ (GeV/c)^2 or less], a large $-t$ break [$t \approx -6.5$ (GeV/c)^2] and two intermediate breaks [$t \approx -1.7$ and -4.1 (GeV/c)^2]. These correspond to dibaryon masses of about 2.2, 2.6, 3.4, and 3.9 GeV/c^2.

In a further attempt to interpret the breaks in the 90° cross section, we have performed a Regge calculation which predicts the energies at which dibaryon resonances might occur.[30] We assume exchange degeneracy and duality. The resonance amplitude is assumed to be represented by the amplitude for exchange of t-channel Regge poles. A partial-wave projection of the Reggeized s-channel amplitudes is then made assuming that the residue functions are essentially independent of t. In the spirit of the calculation, maxima in the imaginary parts of these amplitudes are taken to represent dibaryon resonances. We have not yet looked separately at the real parts of the amplitudes to attempt to obtain Schmid loops.[31]

The choice of parametrization of the s-channel helicity amplitudes[32] parallels the earlier work of Rarita *et al.*[33] In extending their parametrization away from the diffraction peak we were forced to alter the form of the helicity amplitudes due to the restrictions imposed by crossing symmetry and by the Pauli principle. As in Rarita *et al.*,[33] the P, P', and ω poles are assumed to dominate in the cross-channel exchange. The duality assumption permits the neglect of the Pomeranchuk in the parametrization. The effects of the other trajectories which can be exchanged in the t channel (e.g., ρ, φ, A_2) are believed to be sufficiently small so that they can be neglected.

We assume the trajectories have the same intercept and slope, and make the partial-wave projections by numerical integration of the imaginary parts of the complex amplitudes. This results in the reduction to a set of (imaginary parts of) amplitudes representing the scattering in states of definite angular momentum, as functions of the incident momentum. Maxima in these amplitudes are then taken in the model as evidence for the existence of resonances in the p-p system.

In Fig. 14, we again show the $\theta_{c.m.} = 90°$ cross section, with the locations of the above maxima indicated by arrows. The notation used to specify the amplitudes is identical to that of Ref. 32. As shown, in the immediate vicinity of the sharp discontinuities at $-t \approx 6.5$ (GeV/c)^2, we observe max-

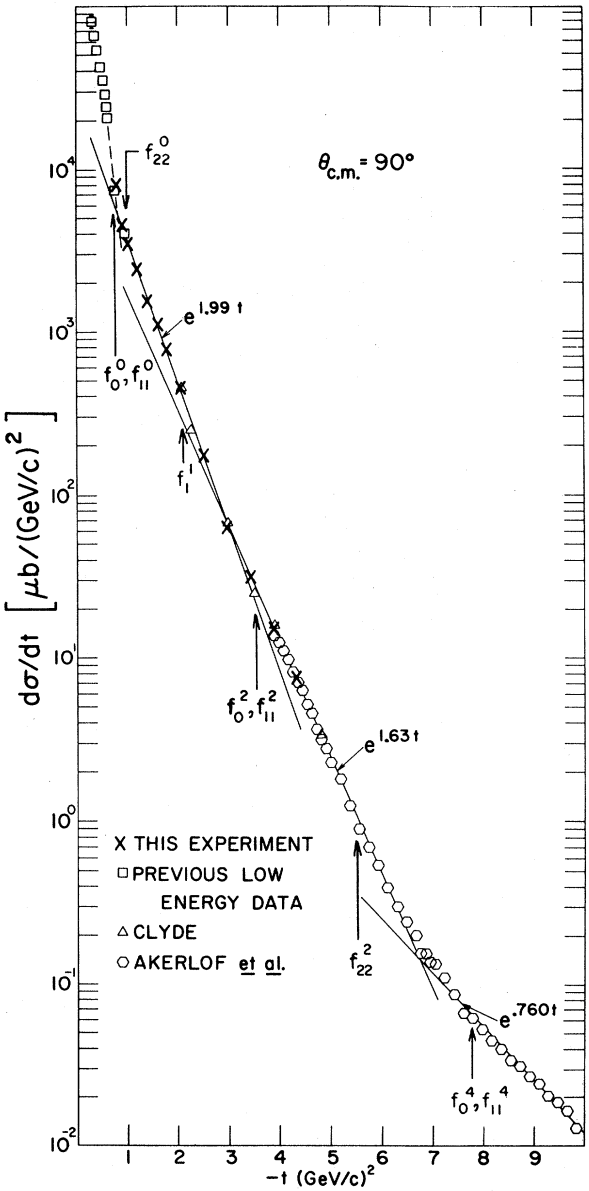

FIG. 14. Differential cross section in p-p elastic scattering at $\theta_{c.m.} = 90°$. Positions of maxima in the calculated s-channel partial-wave amplitudes are indicated by arrows. The notation for the amplitudes is the same as that defined in Ref. 32.

ima in three of the amplitudes. We find maxima approximately equally spaced about the discontinuity near $-t=0.8$ (GeV/c)^2. In the intermediate region, maxima are also found, spaced equally on either side of the observed break at $-t=3$ (GeV/c)^2. A possible interpretation[34] of these latter two breaks is then that they result from the compound effects of adjacent maxima.

ACKNOWLEDGMENTS

We would like to thank the Zero Gradient Synchrotron staff for their generous assistance and cooperation during the experiment. We would also like to express our gratitude to the many people who aided during the performance of the experiment. Among these are Professor J. Mott, Professor K. Galloway, and Dr. King Foo Suen. We appreciate the contributions of Alan Barnes and Peter Coons during the data analysis. We thank Professor Enrico Predazzi and Professor Donald Lichtenberg for many invaluable discussions regarding the interpretation of the data. One of us (H.A.N.) would also like to acknowledge the hospitality of the Aspen Center for Physics during the preparation of a portion of this manuscript.

---

*Work supported in part by the U. S. Atomic Energy Commission under Contract No. AT(11.1)-2009, Task A, and the Indiana University Foundation.

†Portions of this paper are from a dissertation submitted to Indiana University by R. C. Kammerud in partial fulfillment of the degree of doctor of philosophy.

‡Present address: Department of Physics, The Ohio State University, Columbus, Ohio.

§Alfred P. Sloan Foundation Fellow.

‖Present address: Department of Physics, Indiana University-Purdue University at Indianapolis, Indianapolis, Ind.

**Present address: CERN, Geneva 23, Switzerland.

[1]H. A. Neal and M. J. Longo, Phys. Rev. 161, 1374 (1967).

[2]N. E. Booth, G. Conforto, R. J. Esterling, J. Parry, J. Scheid, D. Sherden, and A. Yokasawa, Phys. Rev. Letters 21, 651 (1968).

[3]D. V. Bugg, D. C. Salter, G. H. Stafford, R. F. George, K. F. Riley, and R. J. Tapper, Phys. Rev. 146, 980 (1966).

[4]J. V. Allaby, G. Cocconi, A. N. Diddens, A. Klovning, G. Matthiae, E. J. Sacharidis, and A. M. Wetherell, Phys. Letters 25B, 156 (1967).

[5]J. V. Allaby, A. N. Diddens, A. Klovning, E. Lillethun, E. J. Sacharidis, K. Schlupmann, and A. M. Wetherell, Phys. Letters 27B, 49 (1968).

[6]J. V. Allaby, F. Binon, A. N. Diddens, P. Duteil, A. Klovning, R. Meunier, J. P. Peigneux, E. J. Sacharidis, K. Schulmann, M. Spighel, J. P. Stroot, A. M. Thorndike, and A. M. Wetherell, Phys. Letters 28B, 67 (1968).

[7]The final results from the CERN experiments (Refs. 4–6) are summarized in E. J. Sacharidis, Rutherford High Energy Laboratory Report No. 186, 1969 (unpublished).

[8]C. W. Akerlof, R. H. Hieber, A. D. Krisch, K. W. Edwards, L. G. Ratner, and K. Ruddick, Phys. Rev. 159, 1138 (1967).

[9]B. B. Brabson, R. R. Crittenden, R. M. Heinz, R. C. Kammerud, H. A. Neal, H. W. Paik, R. A. Sidwell, and K. F. Suen, Phys. Rev. Letters 23, 1306 (1969).

[10]A. R. Clyde, Lawrence Radiation Laboratory Report No. UCRL-16275, 1966 (unpublished).

[11]C. M. Ankenbrandt, A. R. Clark, B. Cork, T. Elioff, L. T. Kerth, and W. A. Wenzel, Phys. Rev. 170, 1223 (1968).

[12]R. Wilson, *The Nucleon-Nucleon Interaction, Experimental and Phenomenological Aspects* (Interscience, New York, 1963), and references cited therein.

[13]S. Fernbach, R. Serber, and T. B. Taylor, Phys. Rev. 75, 1352 (1949).

[14]B. Cork, W. Wenzel, and C. Causey, Phys. Rev. 107, 859 (1957).

[15]G. Smith, H. Courant, E. Fowler, H. Kraybill, J. Sandweiss, and H. Taft, Phys. Rev. 123, 2160 (1961).

[16]L. Durand, III, and R. Lipes, Phys. Rev. Letters 20, 637 (1968).

[17]A. D. Krisch, Phys. Rev. Letters 11, 217 (1963).

[18]A. D. Krisch, Phys. Rev. 135, B1456 (1964).

[19]A. D. Krisch, in *Lectures in Theoretical Physics*, edited by W. E. Brittin (Univ. of Colorado Press, Boulder, Colo., 1966), Vol. IX, p. 1.

[20]A. D. Krisch, Phys. Rev. Letters 19, 1149 (1967).

[21]J. Orear, Phys. Letters 13, 190 (1964).

[22]R. Hagedorn, Nuovo Cimento Suppl. 3, 147 (1965).

[23]R. Hagedorn, Nuovo Cimento Suppl. 6, 311 (1968).

[24]R. Hagedorn and J. Ranft, Nuovo Cimento Suppl. 6, 169 (1968).

[25]S. Pinsky, Phys. Rev. Letters 21, 1776 (1968).

[26]H. Fleming, A. Giovani, and E. Predazzi, Ann. Phys. (N.Y.) 54, 62 (1969).

[27]F. Cerulus and A. Martin, Phys. Letters 8, 80 (1964).

[28]L. Marshall Libby, Phys. Letters 29B, 345 (1969).

[29]L. Marshall Libby and E. Predazzi, University of Colorado report, 1969 (unpublished).

[30]The calculation described herein was performed at the suggestion of and with the aid of Professor Enrico Predazzi.

[31]C. Schmid, Phys. Rev. Letters 20, 689 (1968).

[32]M. Goldberger, M. Grissaru, S. MacDowell, and D. Y. Wong, Phys. Rev. 120, 2250 (1960).

[33]W. Rarita, R. Riddell, Jr., Ch. Chiu, and R. Phillips, Phys. Rev. 165, 1615 (1968).

[34]E. Predazzi (private communication).